


Radio-frequency ac Zeeman force for ultracold atoms

A. P. Rotunno¹, W. Miyahira¹, S. Du, and S. Aubin^{1,*†}

Department of Physics, College of William and Mary, Williamsburg, Virginia 23187, USA

 (Received 23 January 2024; accepted 4 November 2024; published 23 December 2024)

We measure the ac Zeeman force acting on ultracold ^{87}Rb atoms due to a radio frequency (rf) field driving intramanifold Zeeman transitions near 8 MHz. We observe about 2.5 times the force of gravity for ≈ 14 mW of rf power acting on atoms ≈ 100 μm from the atom chip. Our measurements are consistent with theoretical predictions and demonstrate the spin-state dependence of the force, as well as its resonant and bipolar behavior. We demonstrate the ac Stern-Gerlach effect by spatially separating a spin mixture, using initial detuning to determine which spins are ac Zeeman high- and low-field seekers. With an eye towards using this force for atom trapping, we observe the time dependence of dressed state spin mixing as a function of detuning and power.

DOI: [10.1103/PhysRevA.110.063321](https://doi.org/10.1103/PhysRevA.110.063321)

I. INTRODUCTION

Atom chips typically trap and manipulate ultracold atoms using magnetic forces and potentials generated by dc currents. However, these dc Zeeman potentials divide an atom's hyperfine spin states into two *fixed* categories: high-field seekers and low-field seekers. Only the latter can be trapped magnetically, since only dc magnetic minima are possible in free space due to Earnshaw's theorem, thus limiting experimental control. Furthermore, the confinement of a typical magnetic trap weakens substantially if the magnetic bias field (trap bottom) is increased to the scale at which many Feshbach resonances occur, thus limiting the degree to which atom-atom interactions can be easily controlled.

The ac Zeeman (ACZ) effect [1–4], based on ac magnetic near fields, provides an alternate and more flexible spin-dependent mechanism for applying magnetic forces on atoms. At low dc magnetic field, the dc Zeeman splittings of neighboring hyperfine spin states are roughly equal and Zeeman transitions between these can be driven with MHz-range radio-frequency (rf) magnetic fields. The corresponding ACZ energy shift is resonant and bipolar, so that any spin state can be a high- or low-field seeker, depending on the rf detuning. Furthermore, the rf field gradient necessary for producing a significant force is independent of the dc field, enabling operation at high magnetic fields.

These rf ACZ potentials are conveniently spin-dependent and straightforward to generate, since MHz-range rf can be easily coupled into an atom chip wire with good efficiency. However, the rf ACZ potential generally affects all of the hyperfine spin states and cannot be targeted at a single spin state. In contrast, a microwave ACZ potential based on a hyperfine transition (typically GHz range) can be targeted at a single pair of spin states [3], although efficiently coupling microwaves into chip wires is challenging [4].

Looking forward, atom chip-based rf ACZ potentials could provide a mechanism for generating spin-dependent potentials for trapped atom interferometry [5], spin-squeezing [6], quantum information, and one-dimensional (1D) many-body physics experiments. Furthermore, the ability of ACZ potentials to manipulate most hyperfine spin-states at arbitrary dc magnetic field opens up the possibility of employing atom chip traps for Feshbach resonance experiments. Finally, ACZ potentials are expected to substantially suppress the potential roughness encountered in dc atom chips [7,8].

We note that rf ACZ potentials can be viewed as rf adiabatic potentials [9,10] in the limit of a strong inhomogeneous rf field and a uniform dc magnetic field. In practice, rf adiabatic potentials typically use a rf field to control the force that a dc magnetic field gradient applies to an atom [8,9,11,12]. In contrast, rf ACZ potentials use a homogeneous dc magnetic field and produce a force using the rf field gradient.

In this paper, we study this rf ACZ force by driving intramanifold Zeeman transitions in ultracold ^{87}Rb atoms with an rf magnetic near field generated by an atom chip. Section II reviews the theory for the ACZ effect in a five-level ladder system. In Sec. III, we describe our experimental system and show that our measurements of the ACZ force are in good agreement with theory. Furthermore, we use this ACZ force to demonstrate the ac Stern-Gerlach effect. With an eye towards an ACZ trap demonstration [13], Sec. IV presents a study of the time evolution of rf-dressed spin states. Finally, Sec. V concludes and provides an outlook for future work.

II. THEORY

In this section, we present the theory of the ac Zeeman effect for a spin-2 five-level ladder system driven by a single rf magnetic field. In essence, the conventional dc magnetic Zeeman Hamiltonian term $H_{\text{DCZ}} = -\vec{\mu} \cdot \vec{B}_{\text{dc}}$ is extended to rf fields as $H_{\text{ACZ}} = -\vec{\mu} \cdot \vec{B}_{\text{rf}}$. In the case of rf close to the frequency of a Zeeman transition, the ACZ effect results in resonant and bipolar energy shifts. If this rf magnetic field

*Contact author: saubi@wm.edu

†<https://saubi.people.wm.edu/>

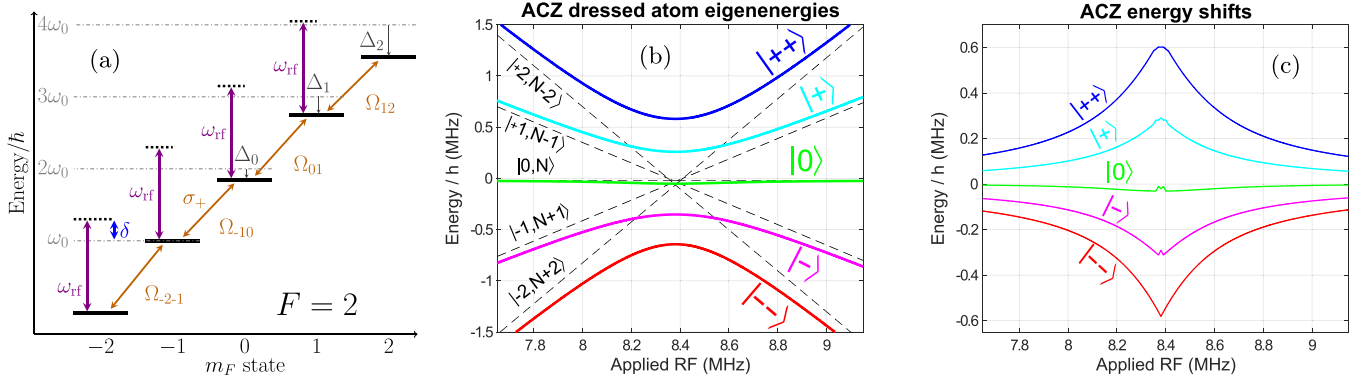


FIG. 1. Theory of rf ACZ potentials in a five-level ladder system. (a) Energy-level diagram for the $5S_{1/2}F=2$ hyperfine manifold of the ^{87}Rb ground state. The five m_F levels are split by a modest dc magnetic field B_{dc} . The splittings are nearly equal, and $\Delta_{\{012\}}$ are the small nonlinear deviations of the $m_F = 0, 1, 2$ levels from the ladder spacing defined by the two lowest levels. A magnetic field oscillating at angular frequency ω_{rf} drives transitions with Rabi frequencies Ω_{m_F, m_F+1} between adjacent m_F states. (b) Calculated ACZ eigenenergy curves versus rf frequency f_{rf} for typical experimental conditions, i.e., $\Omega_0 = 2\pi \times 1.224 \text{ MHz} \approx (0.9 \text{ G})(\mu_B/\hbar)$ and $B_{dc} = 11.98 \text{ G}$ with $\Delta_{\{012\}} = 2\pi \times \{-20.789, -62.213, -124.12\} \text{ kHz}$. Eigenenergies are plotted as colored curves and energies of the bare states ($\Omega_0 \rightarrow 0$) as black dashed lines. (c) Calculated ACZ energy shifts $E_{ACZ,i}$, i.e., difference in energy between ACZ eigenstates and bare states, matching parameters with panel (b). The small central structures are due to the bare state lines crossing at multiple points near 8.375 MHz.

has a gradient in amplitude, then the ACZ energy shift can produce either a weak-field seeking or a strong-field seeking force on the atom.

We consider the five m_F Zeeman states in the $F=2$ hyperfine manifold of the $5S_{1/2}$ ground level of ^{87}Rb . A dc magnetic field $B_{dc}\hat{z}$ of several Gauss defines the quantization axis and separates the five m_F states almost linearly. The dc Zeeman energy separation between adjacent pairs of m_F states is given by $\Delta E_{DCZ} \approx g_F \mu_B B_{dc} \approx 0.7 \text{ MHz/G}$, where $g_F \approx \frac{1}{2}$ is the Landé g factor, and μ_B is the Bohr magneton. Magnetic transition amplitudes between neighboring states $\langle m_F | -\vec{\mu} \cdot \vec{B}_{rf} | m_F \pm 1 \rangle$ are proportional to the applied rf magnetic field B_{rf} , and the atom's magnetic moment $\vec{\mu}$. As shown in Fig. 1(a), the m_F states form a five-level ladder system, which is a more complicated version of the two-level ACZ system studied previously [3,14]. Similar multilevel systems have been extensively studied in the context of adiabatic rf potentials [10,15,16] and rf evaporation [17]. Notably, only $\sigma+$ transitions are allowed within the $F=2$ manifold, the spontaneous emission rate is essentially zero, and electric transitions are forbidden.

For convenience, we define all of the near-resonant energy-level differences relative to the energy separation of the two lowest levels: $E_{-1} - E_{-2} \equiv \hbar\omega_0 = hf_0$, where $h = 2\pi\hbar$ is

Planck's constant. The detuning δ of the rf driving field is defined by the rf frequency $\omega_{rf} = 2\pi f_{rf}$ relative to ω_0 , that is $\delta \equiv \omega_{rf} - \omega_0$. The energy deviations $\Delta_{\{012\}}$ (due to small quadratic Zeeman shifts) of the remaining three states $m_F = \{0, 1, 2\}$ from a perfect energy ladder are defined using multiples of ω_0 : $\Delta_0 = (E_0 - E_{-2})/\hbar - 2\omega_0$, $\Delta_1 = (E_1 - E_{-2})/\hbar - 3\omega_0$, and $\Delta_2 = (E_2 - E_{-2})/\hbar - 4\omega_0$, with $\Delta_{\{012\}} \lesssim 0$, as illustrated in Fig. 1(a).

In a dressed atom picture [14,16,18], we consider a rf field of $N \gg 1$ photons at angular frequency ω_{rf} and local amplitude $\vec{B}_{rf}(x, y)$ that drives the atoms. Individual atoms can absorb from or emit into the rf field, changing m_F level by ± 1 and photon number by ∓ 1 , without significantly changing the field amplitude ($N \pm 1 \simeq N$). We use the five nearly degenerate atom plus photon states as a basis for the atom-field system: $|m_F, N - m_F\rangle = \{|+2, N-2\rangle, |+1, N-1\rangle, |0, N\rangle, |-1, N+1\rangle, |-2, N+2\rangle\}$. The energies of these five states are linear with rf frequency, shown as dashed black lines in Fig. 1(b). These state energies all cross at nearly the same frequency, with offsets due to small nonlinearities in the dc Zeeman shifts (Paschen-Back effect).

After applying the rotating wave approximation [16,19], the Hamiltonian for the atom-field system (in the bare state basis) is given by

$$\frac{H_{\text{tot}}}{\hbar} = \begin{pmatrix} -2\delta + \Delta_2 & \Omega_{12}/2 & 0 & 0 & 0 \\ \Omega_{12}^*/2 & -\delta + \Delta_1 & \Omega_{01}/2 & 0 & 0 \\ 0 & \Omega_{01}^*/2 & \Delta_0 & \Omega_{-10}/2 & 0 \\ 0 & 0 & \Omega_{-10}^*/2 & \delta & \Omega_{-2-1}/2 \\ 0 & 0 & 0 & \Omega_{-2-1}^*/2 & 2\delta \end{pmatrix}. \quad (1)$$

The five-level ladder consists of a chain of four two-level interactions driven by distinct Rabi frequencies. For two m_F states $m < m'$, the Rabi frequency given by

$\Omega_{mm'} = \langle m | -\vec{\mu} \cdot \vec{B}_{rf} | m' \rangle$ can be simplified to $\Omega_{mm'} = -\frac{\mu_B g_F}{2\hbar} \langle m | S_+ B_{rf,-} | m' \rangle$, with spin raising operator $S_{\pm} = S_x \pm iS_y$, circular polarized rf field $B_{rf,\pm} = B_{rf,x} \pm iB_{rf,y}$, and

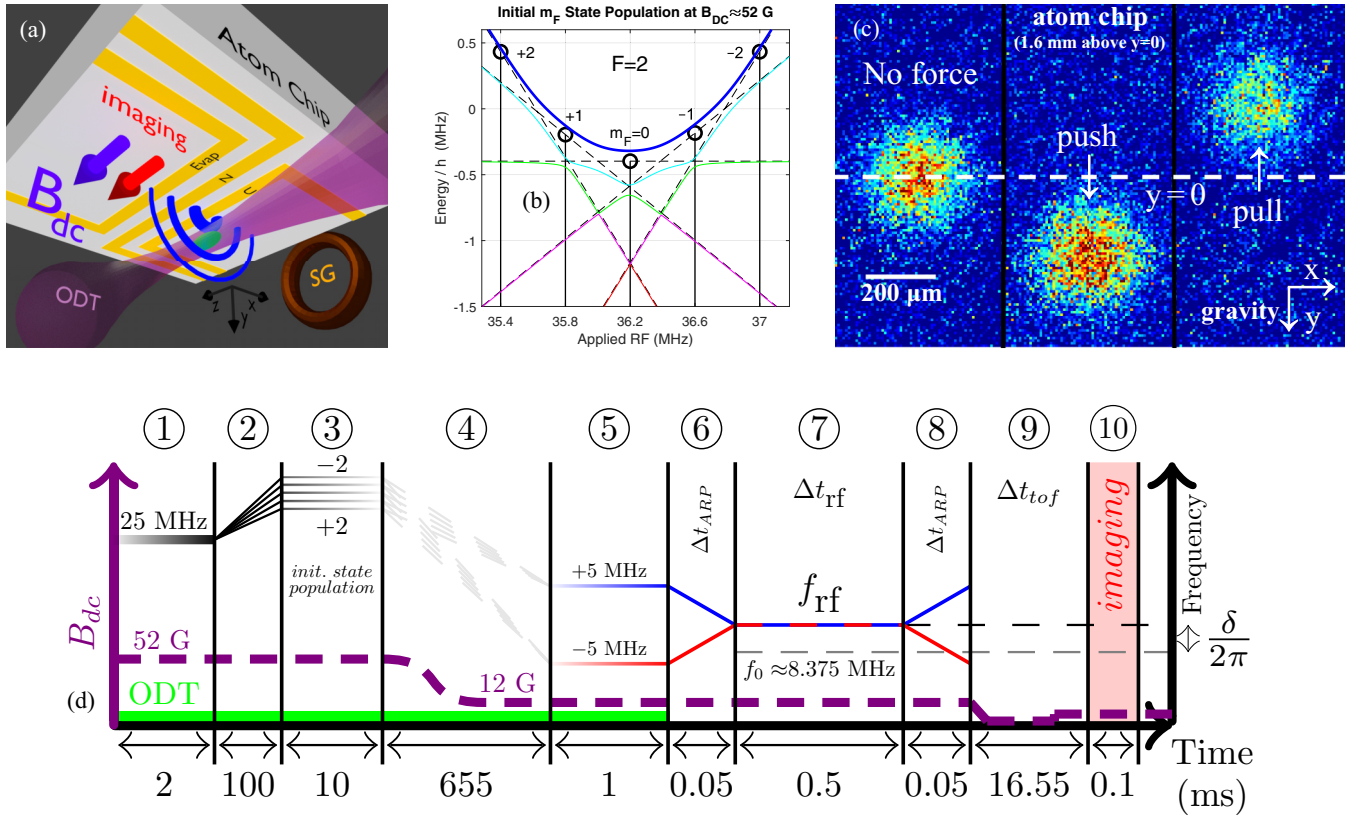


FIG. 2. Experimental setup, atomic state preparation, and ACZ force measurement scheme. (a) Basic experimental setup, not to scale. The cold atom cloud (green) is held in an optical dipole trap (purple), which is aligned along the \hat{z} axis and below the central segment of the U wire (yellow) of the atom chip carrying an rf current I_{rf} . A near-perpendicular \hat{x} -oriented trapping laser beam is omitted for clarity. This rf current generates B_{rf} (semicircular blue field lines), whose gradient creates a force in the $\pm\hat{y}$ direction at the location of the atoms. A uniform dc magnetic field B_{dc} is oriented in the \hat{z} direction, providing a quantization axis. The dc Stern-Gerlach coil (SG) generates a pulsed magnetic gradient for separating spin states along the \hat{x} axis during imaging. (b) Plot of the dressed energy curves used for initial-state preparation at $B_{dc} = 51.745$ G ($\Omega_0 = 2\pi \times 331$ kHz). The $|++\rangle$ dressed energy curve (thick blue) is labeled at the “drop-off” frequencies (black vertical lines and circle markers) used for selectively populating a given initial m_F state. (c) Absorption images of atom clouds showing the maximum “push” and “pull” vertical displacements from Fig. 3 due to the ACZ force with respect to the case of no applied force. (d) Timing diagram for the ACZ force measurements shown in Fig. 3 (see description in text).

electron g factor $g_s = 2$.¹ Only $\sigma+$ transitions are allowed, and these are driven by a $B_{rf,-}$ circularly polarized rf magnetic field. The $B_{rf,+}$ and $B_{rf,z}$ components of the rf field cannot drive transitions within the $F = 2$ manifold.

We define the “Rabi strength” $\Omega_0 = \mu_B |B_{rf,-}|/\hbar$ to describe the ACZ couplings with a single parameter. The matrix elements $\langle F, m | S_+ | F, m' \rangle$ between adjacent m_F states are calculated from the Clebsch-Gordan decomposition of the m_F states in the basis of nuclear and electron-spin states. In the low magnetic-field limit, for the $F = 2$ Zeeman transitions, we have $\langle 2, m | S_+ | 2, m' \rangle = \hbar \sqrt{(2+m)(2-m')}/4\delta_{m,m'+1}$ that then yields²

$$\Omega_{12} = \Omega_{-2,-1} \approx \Omega_0/2 \quad \Omega_{01} = \Omega_{-1,0} \approx \sqrt{3/8}\Omega_0.$$

¹We have neglected the contribution of the nuclear spin to the magnetic moment, which is then given by $\vec{\mu} = (g_s \mu_B/\hbar)\vec{S}$.

²We use the low magnetic-field limit Clebsch-Gordan decomposition for $|F, m_F\rangle$ states, which is exact for $B_{dc} = 0$. At $B_{dc} \approx 12$ G, we estimate that $\langle 2, m | S_+ | 2, m' \rangle$ matrix elements computed from this approximation are accurate to better than 0.5%.

Diagonalizing the Hamiltonian in Eq. (1) across a range of rf detunings results in a five-level avoided crossing, as shown by the eigenenergy curves in Fig. 1(b). We label the corresponding eigenstates $|i\rangle$ (i.e., dressed states) as $\{|++\rangle, |+\rangle, |0\rangle, |-\rangle, |--\rangle\}$, in order from highest to lowest energy. As shown in Fig. 1(c), the actual ACZ energy shift $E_{ACZ,i}$ for each corresponding dressed state $|i\rangle$ is given by the difference between the eigenenergy and the bare energy [i.e., the corresponding dot-dashed black lines in Fig. 1(b), where $\Omega_0 \rightarrow 0$]. At low rf field strength, the atom has four distinct resonances, which then broaden and meld into a single resonance structure [see Fig. 1(c)] as the rf strength increases, i.e., when $|\Omega_0| \gg \Delta_{(012)}$. Furthermore, at low magnetic field B_{dc} , the dc Zeeman splittings are such that $\Delta_2 \approx 2\Delta_1$, resulting in a largely frequency-symmetric eigenenergy plot, see, e.g., Fig. 1(b) and also Figs. 2(b) and 6(b). Appendix A discusses the five level degenerate ladder system (i.e., with $\Delta_{(012)} = 0$).

Far from the central resonance [at 8.375 MHz in Figs. 1(b) and 1(c)], each of the dressed states $|i\rangle$ projects back to a single m_F bare state. An atom prepared in an m_F state far from

resonance can be mapped onto its corresponding $|i\rangle$ dressed state by adiabatically following an eigenenergy curve, i.e., an adiabatic rapid passage, by sweeping the detuning slowly such that $|\frac{d}{dt}\delta| \ll |\Omega|^2$ [20]. Importantly, the initial state and sign of the detuning determine the final dressed state $|i\rangle$, and thus whether the dressed energy increases or decreases. For example, as can be seen in Fig. 1(b), an atom in $m_F = 2$ that begins with f_{rf} well above (below) resonance will map onto $|--\rangle$ ($|++\rangle$) as f_{rf} is brought closer to resonance and will thus experience a downward (upward) ACZ energy shift $E_{\text{ACZ},--}$ ($E_{\text{ACZ},++}$).

If the rf field strength varies spatially, then the ACZ energy shift $E_{\text{ACZ},i}$ will vary in space as well and result in an ACZ force, $\vec{F}_{\text{ACZ},i} = -\vec{\nabla}E_{\text{ACZ},i}$, which pushes atoms to regions of lower ACZ energy. In this work, a rf current in a wire trace on our atom chip generates a spatially varying rf field that falls off roughly as $1/r$, where r is the wire-atom distance. The atoms are attracted or repelled by the wire, depending on the atom's dressed state. The $|-\rangle$ and $|--\rangle$ states experience a negative ACZ energy shift in a rf field and so are strong-field seekers, i.e., they are attracted to the rf wire. In contrast, the $|+\rangle$ and $|++\rangle$ states experience a positive ACZ energy shift, and so are weak-field seekers. These weak-field seeking states are repelled by the rf wire and, in principle, are trappable at a rf magnetic near-field minimum [13].

III. FORCE EXPERIMENTS

In this section, we present our experimental setup, measurements of the rf ACZ force, and the associated ‘‘ac Stern-Gerlach effect.’’ In brief, we apply a short (<1 ms) rf impulse in an atom chip wire to impart momentum to the atom cloud and measure the change in position after a time-of-flight. We find that our measurements agree well with the five-level theory of the rf ACZ force presented in Sec. II. Appendix B describes measurements of the Rabi frequency and its gradient.

A. Experimental setup

We prepare our ultracold sample of ^{87}Rb atoms in an optical dipole trap (ODT) via a multistep cooling and trapping process [21]. Briefly, the atoms are laser cooled in a magneto-optical trap, transferred to a dc Z-wire trap on an atom chip in a separate vacuum chamber, cooled by forced rf evaporation, and finally loaded into the ODT in the $|F = 2, m_F = 2\rangle$ state. A uniform magnetic field B_{dc} directed along the long central section of the Z-wire provides a spin-quantization axis along the \hat{z} direction [see Fig. 2(a)]. We typically load 3×10^5 atoms with a temperature of 350 nK, using a thermal cloud above the BEC transition temperature.

The ODT laser trap is spin-independent and is formed by two focused laser beams at 1064 nm with a combined power of 2 W split 1.2/0.8 into the main (\hat{z}) and cross (\hat{x}) beams, respectively. Both beams are focused under a U-shaped wire [the main beam is illustrated in Fig. 2(c)], and the combined trap is cigar-shaped with the long axis along \hat{z} , which is end-capped by the cross beam. The ODT is located ≈ 100 μm below the U wire and has measured trapping frequencies $\omega_{(x,y,z)} = 2\pi \times (186, 164, 28)$ Hz and a calculated trap depth of 23 μK .

We generate the ACZ potential and force by driving an rf current I_{rf} in the U wire trace on the chip, whose central section is directly above the trapped atoms. The absolute position of the atoms is poorly known, but they are estimated to be 100 to 150 μm below the 50 μm -wide U wire. This rf current (1-50 MHz) generates a rf magnetic near field, shown as blue semicircles centered on the U wire in Fig. 2(c). The oscillating magnetic field at the location of the atoms is \hat{x} -oriented, driving $\sigma+$ transitions around \hat{z} for $F = 2$ atoms, and has an amplitude gradient in the vertical \hat{y} direction, forcing atoms with or against gravity. The atom chip and its rf connections are not impedance matched to the 50 Ω source, and the U-wire impedance is a few Ohms in this frequency range.

The rf source is laboratory-built (based on a AD9910 evaluation board) and generates a phase-continuous signal by direct digital synthesis (DDS) with a microprocessor controller. The rf amplitude is adjusted by an analog voltage variable attenuator (VVA) and is switched on and off quickly (≈ 10 ns) with a high-isolation digital switch. To obtain a rf signal at frequency f_{rf} , the DDS source generates a signal at $100 \text{ MHz} + f_{\text{rf}}$, which we mix down with a high-quality reference at 100 MHz. The down conversion suppresses the second harmonic at $2f_{\text{rf}}$ to -50 dBc, down from -25 dBc at the output of the DDS source.³ Higher-order harmonics from the mixing process are suppressed by a low-pass filter.

Adiabatic rapid passage. Importantly, the rf source is capable of rapid, phase-continuous frequency sweeps for adiabatic rapid passage (ARP) population manipulations. We use ARP sweeps to transfer atoms in an m_F state into a connected dressed state (e.g., $|++\rangle$, $|+\rangle$, etc.), and vice versa. To populate a dressed state, the ARP frequency sweep begins far off-resonance ($|\delta| \gg |\Omega_0|$), so that the bare m_F state maps onto the dressed state that it connects with, following the avoided crossing diagram of Fig. 1(b). The sweep rate is set by reducing it below the point where Landau-Zener transitions to other states are no longer observed.

State preparation. We prepare the atoms in specific m_F states using the sequence outlined in steps (1–4) of the timing diagram of Fig. 2(d). The dc magnetic field is held at $B_{\text{dc}} = 51.745(10)$ G ≈ 52 G, which is large enough to break the Zeeman splittings degeneracy. We perform a low rf power ARP sweep with $\Omega_0 = 2\pi \times 0.3$ MHz to transfer the initial $m_F = +2$ population along the $|++\rangle$ dressed state curve, starting from a large negative detuning, without applying a significant force. By ramping off the rf power at constant frequency, we can ‘‘drop off’’ the atomic population from the $|++\rangle$ state into any m_F state, as illustrated in Fig. 2(b). To populate the $m_F = \{+2, +1, 0, -1, -2\}$ state, we sweep the frequency from 25 MHz to $\{35.4, 35.8, 36.2, 36.6, 37.0\}$ MHz, respectively, for 100 ms before ramping off the rf power adiabatically in 10 ms and lowering B_{dc} to $11.98 \approx 12$ G for the force measurements in Sec. III B.

³Without this suppression, the second harmonic was seen to cause a small force on the atoms for ARP sweeps through the half-resonance frequency.

After preparing the atoms in the chosen m_F state, the atoms are held in the ODT while B_{dc} is ramped down exponentially for 150 ms, then held for 500 ms at ≈ 12 G. This hold time lets any residual motion from a known B_{dc} gradient dissipate.

Due to inelastic collisions during this ODT hold time, as well as imperfect spin state preparation, we observe the following initial spin state purities: For the $m_F = 0$ and $m_F = -1$ initial states, we do not observe the presence of any other spin states. For the stretch state $m_F = +2$ ($m_F = -2$), we detect a population fraction of $\approx 7\%$ of $m_F = +1$ ($m_F = -1$). Finally, when preparing the $m_F = +1$ spin state, $m_F = +2$ atoms are present with a population fraction of 15%. These spin admixtures are relatively small, and we account for them in our data analysis.

ac Zeeman force. An ACZ force is applied to the atoms by subjecting them to an rf magnetic-field gradient (primarily step 7). This process is described in later sections and figures.

Imaging. After dropping from the ODT and applying the ACZ force to the atoms, they undergo a time of flight $\Delta t_{\text{tof}} \approx 16$ ms at a small constant magnetic-field strength to minimize state-dependent curvature from B_{dc} (step 9). Atoms are then imaged on a camera with an absorption probe laser directed along the \hat{z} direction (step 10). Gaussian fits along the x and y axes are used to determine the atom cloud center-of-mass position and atom number. We also perform spin-dependent imaging by using the dc Stern-Gerlach (SG) effect to separate different m_F spin states horizontally ($\pm \hat{x}$) during the time of flight. A copper wire coil, labeled SG in Fig. 2(a), provides a ≈ 7 ms magnetic gradient pulse along the x axis to induce the separation. Atoms with $m_F = +1, +2$ are pushed away from the SG coil ($-\hat{x}$ push), while $m_F = -1, -2$ are pulled closer to the coil ($+\hat{x}$ pull).

B. ac Zeeman-force measurements

Following the method in Ref. [3], we measure the ACZ force by turning off the ODT and applying an rf pulse for a time $\Delta t_{\text{rf}} = 0.5$ ms to impart an impulse $\vec{F}_{ACZ,i} \Delta t_{\text{rf}}$ to the atoms in dressed state $|i\rangle$. Since the atoms are located immediately below the U wire that generates the ac force, the ACZ potential gradient and the impulse are along the vertical y axis. After a time of flight $\Delta t_{\text{tof}} = 16.55$ ms, we measure the difference in atom position Δy_i traveled by the atoms due to the impulse, compared with the same state falling with no impulse. Due to the small atomic cloud size and short Δt_{rf} , the ACZ force is essentially constant in space and time and is

$$F_{ACZ,i} = \frac{m \Delta y_i}{\Delta t_{\text{rf}} \Delta t_{\text{tof}}}. \quad (2)$$

To apply $F_{ACZ,i}$ to a specific dressed state $|i\rangle$, we include short rf ARP sweeps of duration $\Delta t_{ARP} = 0.05$ ms immediately before and after the rf pulse. These ARP frequency sweeps map the initially prepared m_F state onto a dressed state $|i\rangle$, and vice versa, in the following manner: If the rf frequency's initial detuning δ_0 is very far below (above) resonance and is then swept up (down) adiabatically, then the $m_F = -2, -1, 0, 1, 2$ states map onto the $\{|++\rangle, |+\rangle, |0\rangle, |-\rangle, |--\rangle\}$ ($\{|--\rangle, |-\rangle, |0\rangle, |+\rangle, |++\rangle\}$) dressed states in accordance with the eigenenergy curves in

Fig. 1(b). Reversing the sweep returns the atom to the original m_F state. In all cases, the power and rate of ARP frequency sweeps are chosen to avoid Landau-Zener transitions.

The specific experimental sequence for measuring the ACZ force is the following [see Fig. 2(d)]: After preparing the atoms in one of the five m_F states with $B_{dc} = 51.745 \text{ G} \approx 52 \text{ G}$ [steps 1–4 of Fig. 2(d)], see details in Sec. III A, we ramp down the magnetic field to $B_{dc} \approx 12 \text{ G}$. The rf frequency is set to $f_{\text{rf}} \pm 5 \text{ MHz}$ in preparation for the initial ARP sweep, the rf power is ramped on to 13.6 mW over the course of 1 ms, and the ODT is then turned off (step 5). The first ARP sweep ramps the rf frequency to the rf pulse frequency f_{rf} in a time $\Delta t_{ARP} = 0.05 \text{ ms}$ (step 6). During the time $\Delta t = 0.5 \text{ ms}$ of the rf pulse, the atoms are accelerated by the ACZ force (step 7). Next, the ARP sweep is reversed, again with $\Delta t_{ARP} = 0.05 \text{ ms}$, back to the initial rf frequency $f_{\text{rf}} \pm 5 \text{ MHz}$ to return the atoms to their initial m_F state (step 8). Finally, the atoms undergo free fall for a time of flight of $\Delta t_{\text{tof}} = 16.55 \text{ ms}$ (step 9) with B_{dc} reduced to near zero to suppress the effects of its small magnetic gradient on atom position. The free fall is followed by a $100 \mu\text{s}$ absorption image of the cloud to determine the center-of-mass change in the vertical position Δy_i (step 10). Figure 2(c) shows example images of atomic clouds that have been pushed or pulled by the ACZ force for an on-resonance rf pulse, along with a reference image for no applied ACZ force (i.e., $\Delta y_i = 0$).

We measure the displacement Δy_i for all five ACZ eigenstates, from both initial detunings: $\delta_i < 0$, $\delta_i > 0$. Figure 3 shows the measured Δy_i on the left axis versus the applied rf pulse frequency f_{rf} for dressed states populated by an ARP sweep from above [Fig. 3(a)] and below [Fig. 3(b)] the resonance at $f_0 \approx 8.375 \text{ MHz}$. The Δy_i data points and error bars are obtained from a weighted mean of positions extracted from Gaussian fits of atomic cloud images from up to three distinct measurements taken in randomized order.

We see that the $|++\rangle$ and $|+\rangle$ states are weak-field seekers (i.e., pushed away from the rf wire, located at $y < 0$), while the $|--\rangle$ and $|-\rangle$ states are high-field seekers (i.e., pulled towards the rf wire). The $|0\rangle$ state remains largely unperturbed for these power levels. Furthermore, the data in Fig. 3 shows that a high-field seeking *or* a weak-field seeking force can be applied to any $m_F \neq 0$ state depending on whether the starting frequency of the initial ARP sweep is above or below resonance. As with the dc Zeeman case, the initial m_F value scales the magnetic interaction strength, resulting in an ACZ force about twice as strong for the $|++\rangle$ and $|--\rangle$ states as for the $|+\rangle$ and $|-\rangle$ states.

The right axes for the dashed lines of Fig. 3 show the force corresponding to a given displacement, based on Eq. (2). This force conversion does not include the contribution to the impulse from the $50 \mu\text{s}$ ARP sweeps before and after the rf pulse. Notably, the on-resonance ACZ force strength is a little over 2.5 times Earth's gravity, for only 13.6 mW of rf power directed to the chip.

Theoretical predictions based on Eq. (1) are given by the solid, dotted, and dashed line curves in Fig. 3 and are consistent with the data. These theory curves represent *ab initio* predictions for the force $F_{ACZ,i}$ (dashed line, right axis) and displacement Δy_i (solid line, left axis) based on measured values for the Rabi strength $\Omega_0(\vec{r}_0) = 2\pi \times 1.224(3) \text{ MHz}$ and

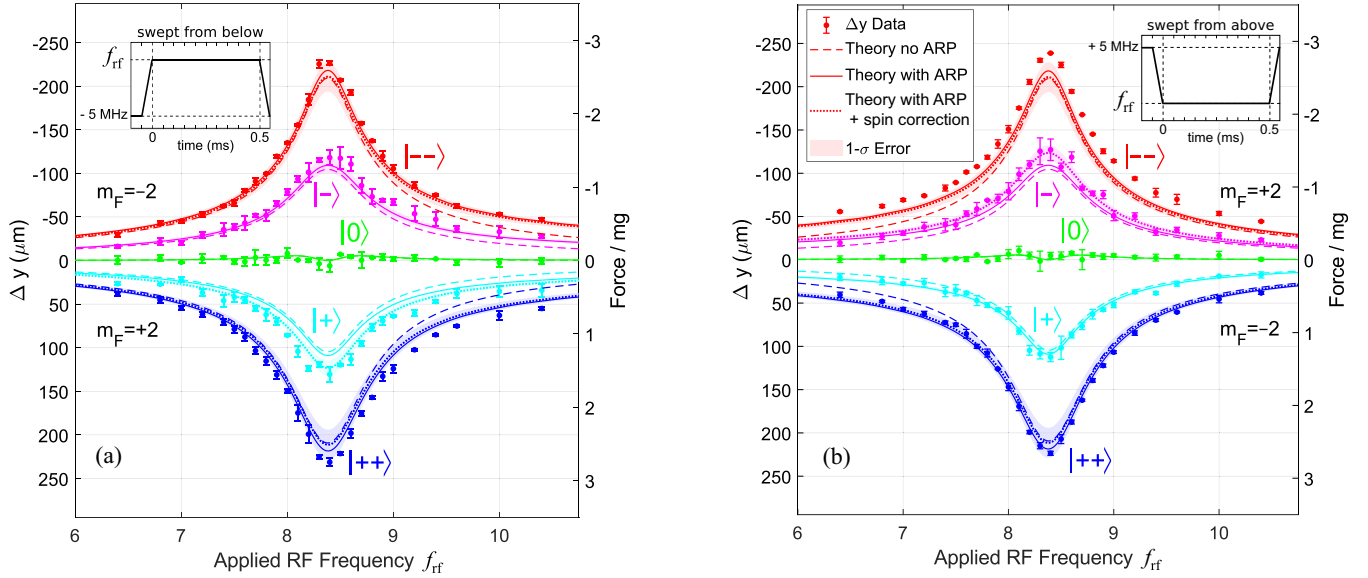


FIG. 3. Comparison of data and theory for the ACZ force measurements. Both plots show the displacement Δy_i (left axis) and corresponding ACZ force $F_{ACZ,i}$ (right axis, with units mg for Earth's gravitational force on a ^{87}Rb atom of mass m) versus rf pulse frequency f_{rf} for the five dressed states. $\Delta y_i = 0$ corresponds to no applied rf ($\Omega_0 = 0$). (a) The dressed states are populated with an initial upward ARP sweep starting at $f_{\text{rf}} - 5$ MHz, as shown in the inset. (b) The dressed states are populated with an initial downward ARP sweep starting at $f_{\text{rf}} + 5$ MHz, as shown in the inset. The theory curves for Δy_i (solid lines) and the ACZ force $F_{ACZ,i}$ (dashed lines) are not fits and use separate measurements of the Rabi strength Ω_0 and its associated gradient $d\Omega_0/dy$. The Δy_i theory curve includes the small displacements due to the pre- and postpulse ARP sweeps. The dotted lines show the expected Δy_i displacements when the spin impurities of the initial spin states are included: these theory curves are calculated by taking a weighted average of the solid line predictions, with the weights given by the initial spin distributions. The $1-\sigma$ shading gives the uncertainty in the Δy_i dotted theory curves due to errors in the Ω_0 and $d\Omega_0/dy$ measurements (see Appendix B).

its vertical gradient $d\Omega_0(\vec{r}_0)/dy = 2\pi \times 10.64(77)$ kHz/ μm at the initial location of the atoms \vec{r}_0 (see Appendix B).⁴ The dotted line is generated from the solid line prediction and represents the expected displacement Δy_i when the initial imperfect spin distribution is included (see Sec. III A).

The ACZ force $F_{ACZ,i}$ is calculated from the gradient along y of the ACZ energy shift $E_{ACZ,i}(f_{\text{rf}}, \Omega_0(y))$:

$$F_{ACZ,i}(\vec{r}_0) = -\left. \frac{d}{dy} E_{ACZ,i}(f_{\text{rf}}, \Omega_0(\vec{r})) \right|_{\vec{r}=\vec{r}_0} \quad (3)$$

$$= -\left. \frac{dE_{ACZ,i}}{d\Omega_0} \right|_{\Omega_0=\Omega_0(\vec{r}_0)} \left. \frac{d\Omega_0(\vec{r})}{dy} \right|_{\vec{r}=\vec{r}_0}, \quad (4)$$

where $dE_{ACZ,i}/d\Omega_0$ is evaluated numerically from the eigenenergies of Eq. (1) using the measured value of $\Omega_0(\vec{r}_0)$. The gradient $d\Omega_0/dy$ is obtained experimentally by slightly adjusting the trap vertical position around $y = y_0$ and measuring the change in Rabi strength Ω_0 (see Appendix B).

The prediction for the displacement $\Delta y_i(f_{\text{rf}})$ includes the contributions from both the rf pulse and the initial and final ARP sweeps. The contribution of the ARP sweeps is evident in the small asymmetry of the data in Fig. 3, where sweeps across resonance display a deviation from the dashed symmetric theory force line. We calculate the $\Delta y_i(f_{\text{rf}})$ prediction

by numerical integration of the theoretical ACZ force over the duration of the rf pulse and ARP sweeps:

$$\Delta y_i(f_{\text{rf}}) = \frac{\Delta t_{\text{tof}}}{m} \int F_{ACZ,i} \left(\delta(t), \Omega_0(t), \frac{d\Omega_0}{dt} \right) dt. \quad (5)$$

The time dependence of $\delta(t)$ is due to the ARP sweeps, and is the primary contribution to the gap between the solid and dashed lines of Fig. 3.⁵ Lesser effects include the time dependence of $\Omega_0(f_{\text{rf}}(t), y(t), t)$, due to sweeping f_{rf} through the unmatched rf coupling into the chip U wire, the dependence on y from the short gravitational free fall during the rf impulse, and the direct dependence on t from transient rf power variations when turning on the rf, although this happens far off resonance. These last three dependencies are relatively small and contribute less than 1% to the total Δy_i .

The shaded bands in Fig. 3 show the $1-\sigma$ uncertainty on the Δy_i displacement prediction curves (dotted lines) due to the measurement errors for Ω_0 and $d\Omega_0/dy$. The largest source of uncertainty is in $d\Omega_0/dy$ due to errors in evaluating small changes in position (see Appendix B). Furthermore, the ODT is known to move with variations in room temperature, typically 5–10 μm vertically over a roughly 1.5 hr timescale and additionally shows long-term drifts on the same length scale.

⁴This Rabi strength corresponds to $B_{\text{rf}} \approx 0.9$ G. If we assume a $1/r$ falloff for B_{rf} away from the U wire, then this value for Ω_0 implies an rf current $I_{\text{rf}} \approx 30$ mA rms.

⁵This effect suggests more generally that, in atom chip experiments, an ARP sweep with a rf field with a strong gradient may significantly impinge a cloud of atoms, when only a population change is expected.

Finally, we include the result of using an initially imperfect spin state, i.e., due to the mixing of $m_F = \pm 2$ into $m_F = \pm 1$, respectively, and $m_F = -1$ into $m_F = -2$. The dotted lines in Fig. 3 are computed by taking a weighted average of the solid line predictions with the weights given by the spin population fraction (see Sec. III A for the spin distributions). The dotted line prediction in Fig. 3 does not differ much from the solid line for the $|+\rangle$ and $|-\rangle$ states. However, in the case of the $|+\rangle$ state in Fig. 3(a) and the $|-\rangle$ state in Fig. 3(b) (both generated by an initial $m_F = +1$ state, with 15% contamination by $m_F = +2$), the dotted line prediction for Δy_i better matches the data.

Overall, we see that the theory curves are generally good predictors for the data. However, we note that the dressed states that are populated with ARP sweeps starting from the $m_F = +2$ state, i.e., the $|+\rangle$ state in Fig. 3(a) and the $|-\rangle$ state in Fig. 3(b), have systematically larger shifts than the theoretical predictions.

C. ac Stern-Gerlach effect

The rf ACZ force can be used to generate an ‘‘ac Stern-Gerlach effect’’ that is more versatile than the original dc Stern-Gerlach effect discovered a century ago [22]. In the dc version of the effect, a dc magnetic gradient is applied to a spin mixture of atoms to spatially separate them according to their quantized spin. In the case of ^{87}Rb , atoms in $F = 2$ with $m_F > 0$ ($m_F < 0$) travel to lower (higher) magnetic fields, which can be used for spin-resolved imaging of spin mixtures [3]. The ac Stern-Gerlach effect operates in a similar manner, except that a near-resonant rf magnetic field gradient is used to generate a spin-dependent ACZ force: Depending on the initial detuning of the rf field sweep, states with $m_F > 0$ can be either high-field or low-field seekers, and vice versa for the $m_F < 0$ states.

We demonstrate the ac Stern-Gerlach effect (see Fig. 4) by modifying the force measurement experiment from Sec. III B into a two-part process. First, starting with atoms in a mixture of m_F states, we use a resonant ACZ force to separate m_F states vertically. The initial detuning of the rf impulse determines whether an m_F state is pulled towards or pushed away from the chip. Second, the dc Stern-Gerlach effect is used to separate the m_F states horizontally for state identification.

The experimental sequence is the following [see Fig. 4(a)]: With $B_{dc} \approx 12$ G, we generate a mixture of all five m_F states in the ODT (step 1), by applying resonant rf for much longer (1 ms) than the Rabi flopping coherence time (about 10 μs). Next, we apply the rf ACZ force impulse used in Sec. III B (steps 2–6). After setting the initial rf frequency to $f_0 \pm 5$ MHz with the rf power off (step 2), we turn on the rf power to 13.6 mW and release the atoms from the ODT (step 3), and apply a brief 50 μs ARP sweep to $f_{rf} = f_0 \approx 8.375$ MHz (step 4). As in the force measurement, this ARP sweep maps each m_F state onto a specific $|i\rangle$ dressed state. Over the duration of the 0.5 ms ACZ force impulse (step 5), each $|i\rangle$ state experiences the resonant force in Fig. 3, with the force direction given by the initial detuning of the ARP sweep. Next, a second 50 μs ARP sweep returns the rf frequency to its initial value $f_{rf} = f_0 \pm 5$ MHz (step 6), thus returning each atom to its original m_F state. In essence, we

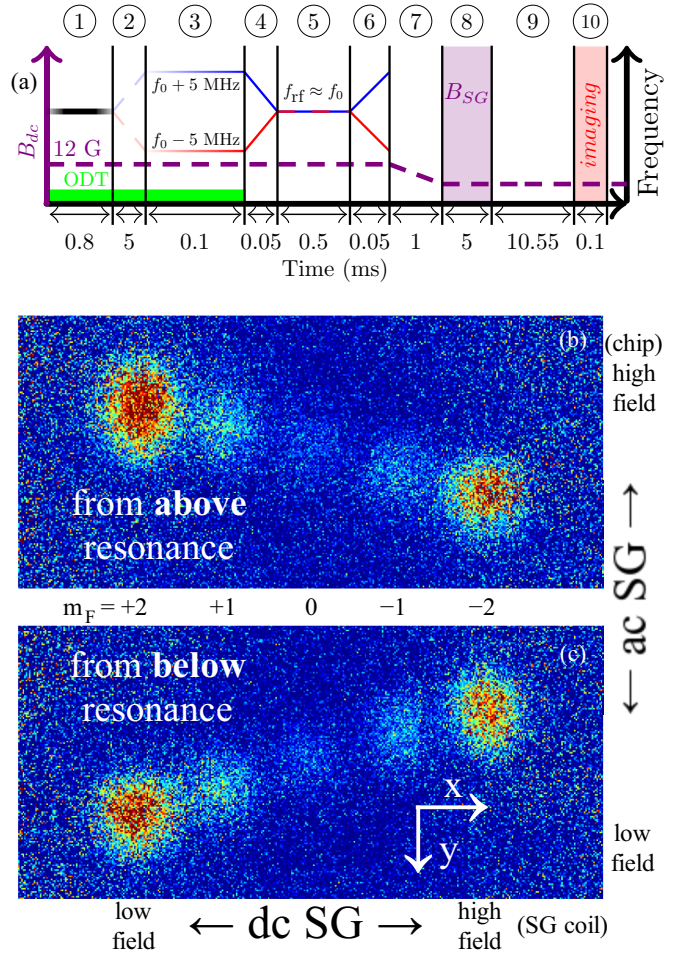


FIG. 4. ac Stern-Gerlach effect. (a) Timing diagram for preparing a spin mixture in the $F = 2$ hyperfine manifold and then applying an ACZ force to separate the spin states vertically (see text for details). (b), (c) Images of the five distinct m_F atomic clouds after undergoing ac Stern-Gerlach separation in the vertical direction due to a vertical rf magnetic gradient and dc Stern-Gerlach horizontal separation due to a horizontal dc magnetic gradient. The images are averages over more than a dozen experimental cycles. (b) For an initial rf detuning above resonance, $m_F > 0$ states are high rf field seekers, and $m_F < 0$ states are low rf field seekers; (c) the roles are reversed for an initial detuning below resonance.

repeat the experimental points of Fig. 3 at $f_{rf} = 8.375$ MHz for all five states simultaneously.

After the vertical ACZ impulse, we reduce B_{dc} to 5 G (step 7) for imaging. Then, we apply a horizontal dc magnetic gradient [using the SG coil in Fig. 2(a)] to separate the m_F states horizontally via the dc Stern-Gerlach effect (step 8). Independent of the ACZ impulse, atoms with $m_F > 0$ ($m_F < 0$) travel to high (low) dc field. Finally, after a time of flight to sufficiently separate the five m_F atomic clouds (step 9), we image the atoms (step 10).

The two images in Figs. 4(b) and 4(c) show that the ac Stern-Gerlach effect works as expected. The ac version of the effect is more versatile than the dc case, since a spin state can be either a low-field or a high-field seeker. For example, the dc high-field seeker $m_F = -2$ ($F = 2$) is always pulled towards a chip dc current but can also be pushed away from the chip

by a rf current. Notably, the first observation of the ac Stern-Gerlach effect required a 1 kW amplifier to generate up to 8 A rms of rf current to deflect the spins of an atomic beam [23], whereas our chip-based approach uses about 13 mW of rf power.

IV. TIME EVOLUTION OF STATES

In this section, we investigate the long-term time evolution of the $|++\rangle$ and $|--\rangle$ dressed states (i.e., their stability) with an eye towards future applications of rf ACZ potentials, such as trapping and spin-dependent manipulations. Specifically, we determine the extent to which the $|++\rangle$ state (or the $|--\rangle$ state) leaks into, or mixes into, the other dressed states. Importantly, we find that the $|++\rangle$ and $|--\rangle$ states show increased stability for an rf frequency further from resonance and for a larger rf field strength. In contrast, on-resonance rf leads to faster leakage out of the initial dressed state, albeit at different rates for $|++\rangle$ and $|--\rangle$. The resonant nature of the leakage is suggestive of spin-changing collisions or Landau-Zener transitions [24,25].

We measure the time evolution by holding the atoms in the ODT and using the same timing sequence as the force measurements (Sec. III B), but with a variable ACZ force application time t_{hold} , as shown in Fig. 5(a). We populate the $|++\rangle$ or $|--\rangle$ state by starting with atoms in either $m_F = 2$ or $m_F = -2$, and the rf frequency at a large detuning, ± 5 MHz. Next, we sweep the rf frequency close to resonance, hold for a variable time, and then sweep the frequency back to its initial detuning value so that the atoms are projected back into the bare m_F states. Finally, we turn off the ODT and the rf and use the Stern-Gerlach imaging from Sec. III C to measure the population in the various m_F states. Notably, we use a reduced rf power of 0.66 mW (a factor of ≈ 20 smaller than for the force measurements in Sec. III B) resulting in a ACZ force that does not forcibly remove atoms from the ODT: The $|++\rangle$ and $|--\rangle$ states experience a -18% and $+19\%$ change to the trap depth, respectively, relative to the case of no applied rf.

Figure 5(b) shows a sample plot of the fractional population of atoms in each m_F state versus the duration of the rf application time for atoms prepared in the $|++\rangle$ state. The atoms in the initially prepared state steadily populate (“mix into”) the adjacent dressed states, and so on until a rough equilibrium across the states is reached.

We define the mixing time $\Delta t_{1/2}$ as the time that it takes the initial slightly mixed dressed state fraction P_{start} to drop to 50% of the total atomic population in the ODT. The total population fraction in the other states (i.e., not the initial state) is given by $P_{\text{other}} = 1 - P_{\text{start}}$. We use $\Delta t_{1/2}$ as a figure of merit for evaluating the timescale over which a future rf trap will potentially confine atoms in a given dressed state. Conveniently, this definition does not depend on the functional form of the time evolution nor on the population in each dressed state, but only on the fractional population distribution. We determine $\Delta t_{1/2}$ by linear fitting of P_{start} versus the logarithm of rf hold time $\log_{10}(t_{\text{hold}})$, taking the crossing of the fit lines for $P_{\text{start}} = 1/2$ ($=P_{\text{other}}$), illustrated in Fig. 5(b). Datasets were hand-bound to exclude the initial constant population period before decay and later low-population points. When $P_{\text{start}} > P_{\text{other}}$ beyond our longest hold time of 3 s, we extrapolate fits for $\Delta t_{1/2}$.

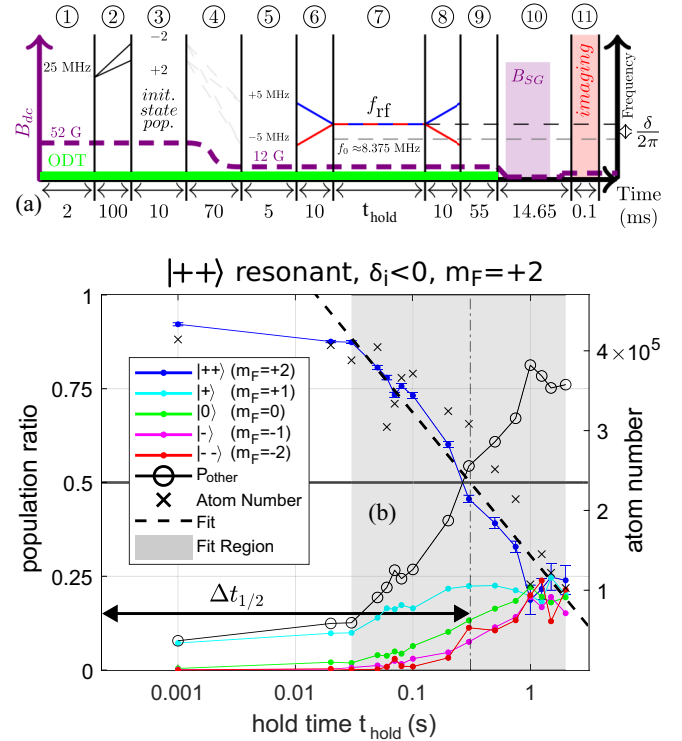


FIG. 5. Time evolution of the dressed states. (a) Timing diagram for the time evolution measurements. Steps 1–8 are similar to those in Fig. 2(d), albeit with variations in the timing. The rf power is ramped off in step 9 in 5 ms, and the Stern-Gerlach imaging method used in Sec. III C is implemented in steps 10 and 11. (b) Time evolution data showing the fractional population in the $|++\rangle$ state (blue, left vertical axis) as a function of the hold time for a resonant $\delta_i = -5$ MHz to atoms initially in $m_F = +2$. The fractional populations in the other dressed states are shown using the same color scheme as Figs. 1(b) and 1(c); the legend shows the corresponding m_F state used for imaging. Here, the $|++\rangle$ state is populated by applying an rf ARP sweep with an initial detuning $\delta_i = -5$ MHz to atoms initially in $m_F = +2$. The black line and circles (\circ , left axis) show the total fractional population that is not in the $|++\rangle$ state. The dashed line shows the interpolation fit (using points in the gray shaded region) for determining the hold time $\Delta t_{1/2}$ at which the fractional population in the $|++\rangle$ state drops to 50%. The total atom number, i.e., the sum of the dressed state populations, is represented with the crosses (\times , right vertical axis).

olate fits for $\Delta t_{1/2}$. In the sections below, we study $\Delta t_{1/2}$ as a function of rf detuning and rf field strength.

We note that the lifetimes for the m_F spin states in the ODT are not equal for our trapping conditions (atom number, temperature, and density). Atoms in the $m_F = +2$ and -2 states have $1/e$ lifetimes of roughly 7 and 5 s, respectively. In contrast, atoms initially prepared in one of the $m_F = 1, 0$, or -1 states have lifetimes just below 1 s, due in part to allowed inelastic spin-changing collisions for these states. Consequently, $\Delta t_{1/2}$ includes the result of the different lifetimes of m_F states in the ODT.

A. Mixing vs detuning

We find that the detuning of the applied rf has a major effect on the rate of state mixing. Figure 6 shows that the mixing

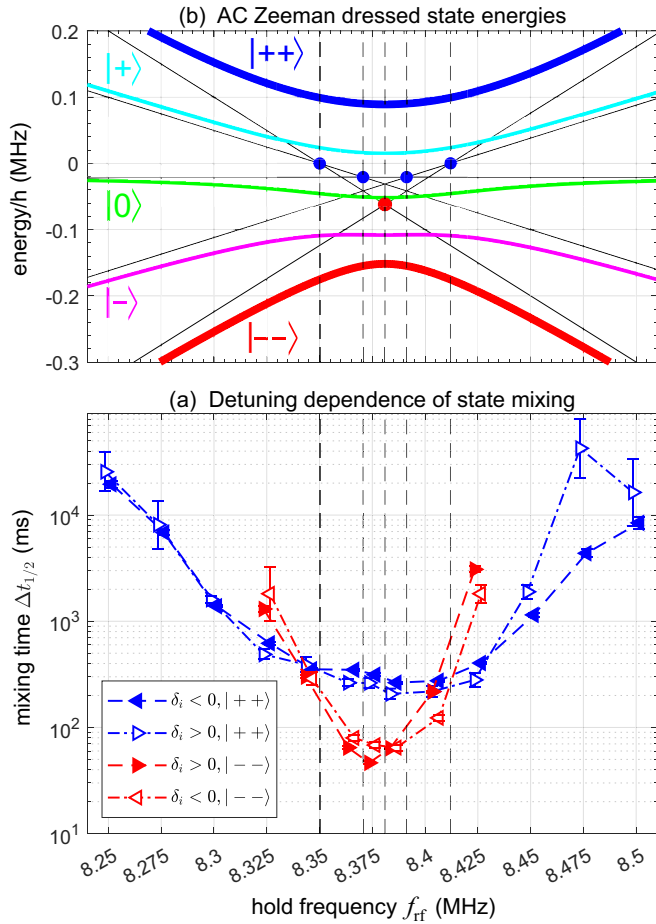


FIG. 6. Dressed state mixing time versus rf frequency. (a) Dressed state mixing time $\Delta t_{1/2}$ measurements versus rf hold frequency f_{rf} for the $|++\rangle$ (blue) and $|--\rangle$ (red) dressed states. The $\Delta t_{1/2}$ values and $1 - \sigma$ errors are obtained from fits to time evolution data, e.g., Fig. 5(b). The data points are slightly offset right and left of the applied f_{rf} for clarity. The two dressed states are populated by using atoms initially in $m_F = +2$ (filled triangles) or $m_F = -2$ (unfilled triangles) and then applying a rf ARP sweep with initial detuning $\delta_i = -5$ MHz (left-pointing triangles) or $\delta_i = +5$ MHz (right-pointing triangles). The rf power is 0.66 mW, corresponding to $\Omega_0 = 2\pi \times 238$ kHz. (b) Calculated ac Zeeman dressed state energies versus hold frequency f_{rf} at $B_{dc} = 11.98$ G. The black lines show the m_F bare state energies. The blue and red circles (\bullet) show the bare state crossings relevant to the $|++\rangle$ and $|--\rangle$ states, respectively. The vertical dashed lines mark the f_{rf} positions for these crossings on both plots.

time $\Delta t_{1/2}$ exhibits a strong reduction near resonance for both the $|++\rangle$ and $|--\rangle$ states, while off resonance the mixing occurs on a much slower timescale. This change in $\Delta t_{1/2}$ is largely symmetric with respect to detuning, in contrast with a similar experiment with microwave ACZ dressed states [3]. We suspect that the resonant behavior is due in part to inelastic collisions of population in the $m_F = -1, 0, 1$ components of the dressed states. Notably, the $|--\rangle$ state shows faster mixing on resonance than its $|++\rangle$ counterpart, while off-resonance it displays slower mixing.

The dressed energies of the $|++\rangle$ and $|--\rangle$ states mirror the detuning behavior of spin mixing for these states

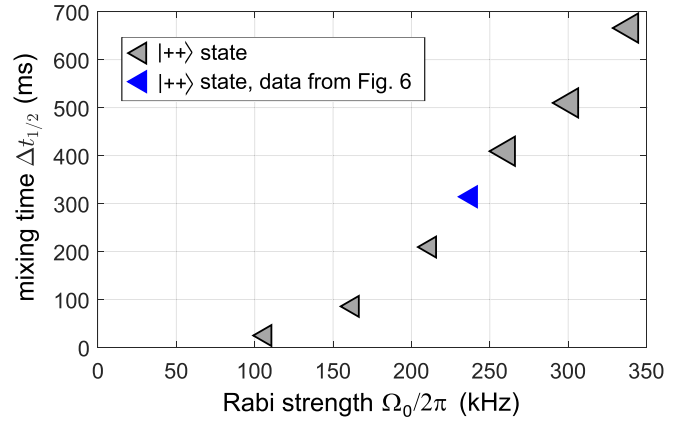


FIG. 7. On resonance mixing time $\Delta t_{1/2}$ versus rf field strength for the $|++\rangle$ dressed state. The $|++\rangle$ state is populated by an ARP sweep of the rf frequency with $\delta_i < 0$ to $f_{\text{rf}} = 8.375$ MHz. The $\Delta t_{1/2}$ values are obtained from linear time fits (small triangles) or logarithmic time fits (large triangles) of state evolution data, e.g., Fig. 5(b). The $1 - \sigma$ error bars are on the order of the vertical triangle size. The Rabi strength Ω_0 is varied by adjusting the rf power. We determine Ω_0 at a given rf power \mathcal{P}_{rf} by scaling down $\Omega_0 = 2\pi \times 1.09$ MHz measured directly at rf power $\mathcal{P}_{\text{rf},0} = 11.36$ mW by $\sqrt{\mathcal{P}_{\text{rf}}/\mathcal{P}_{\text{rf},0}}$.

[Fig. 6(a)], suggesting a link. Figure 6(b) shows that near resonance the $|++\rangle$ state involves four avoided crossing over a detuning span of 60 kHz and is separated in energy from the $|+\rangle$ state by about 75 kHz. In contrast, the $|--\rangle$ state has one avoided crossing with an energy gap of about 45 kHz. While we do not propose a specific mechanism, the resonant spin mixing behavior in Fig. 6(a) suggests that spin changing collisions mix the dressed states, or that other transitions between dressed states are happening inadvertently. Examples of transition mechanisms include magnetic noise in the 30–90 kHz range or Landau-Zener transitions [24,25] due to noise in the dc magnetic field B_{dc} .

B. Mixing vs power

Another major contributing factor to the mixing rate of dressed states is the applied rf power. We study the on-resonance behavior of the low-field seeking $|++\rangle$ state, a prime candidate for rf ACZ trapping, and find that the spin mixing time $\Delta t_{1/2}$ increases with rf field strength by varying the rf power over a 10 dB range. Figure 7 shows that $\Delta t_{1/2}$ increases monotonically with the Rabi frequency Ω_0 , and this dependence tends asymptotically towards a linear one for high Ω_0 , so that $\Delta t_{1/2}$ is maximized by operating at high rf power. The main conclusion is that higher rf powers minimize mixing, while low powers are more prone to it. This behavior is consistent with spin mixing via Landau-Zener transitions across rf power-broadened avoided level crossings between bare states [24,25].

C. Outlook for trapping

In the context of designing a rf ACZ trap [13], the rf detuning and rf field strength studies show that state mixing can be minimized by operating off resonance and with high rf power. In the case of the weak-field seeking $|++\rangle$ state,

these studies show that $\Delta t_{1/2}$ mixing times greater than 1 s are achievable at detunings greater than 100 kHz. Using off resonance rf suppresses the state mixing rate at the cost of a somewhat lower trapping force.

V. CONCLUSION

We have demonstrated the ability to generate a force for neutral atoms using rf near field gradients at MHz frequencies to drive Zeeman transitions within a hyperfine manifold. Measurements of the rf ACZ force are consistent with theoretical predictions based on dressed atom theory. Furthermore, all nonzero m_F states can be high- or low- field seekers, depending on the detuning of the rf field. Notably, low-field seeking states should be trappable if placed in a rf field with a local minimum [13]. Looking toward trapping, we find that the time for the dressed states to mix depends strongly on rf power and detuning: More specifically, a large detuning and a high rf power reduce the mixing rate.

In the broader context of atom chip experiments, a significant rf ACZ force (roughly 2.5 times Earth's gravitational force on a Rb atom) can be applied to atoms in a standard micromagnetic chip trap for a modest rf power (14 mW). Indeed, in the case of a standard micromagnetic chip trap, an on-chip rf evaporation wire is capable of applying a comparable rf ACZ force and thus affecting the evaporative cooling process.

ACKNOWLEDGMENTS

This work was supported by NSF Grants No. PHY-1806558 and No. PHY-2308767 and DTRA Grant No. HDTRA1-19-0027. W.M. acknowledges partial support from the Virginia Space Grant Consortium.

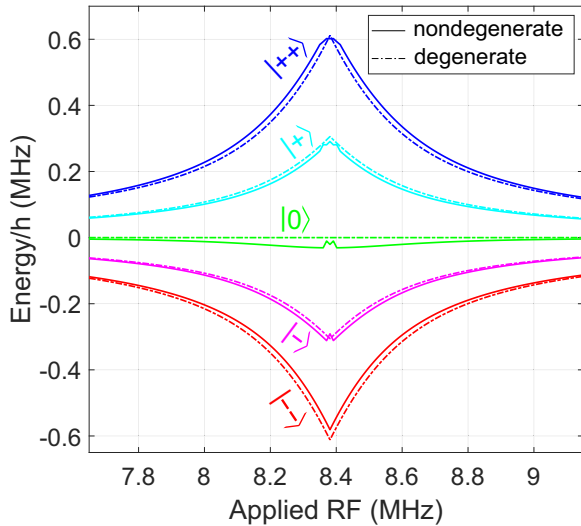


FIG. 8. Comparison of ac Zeeman shifts for dressed states of a nondegenerate five-level ladder (solid) and the degenerate ladder approximation (dot-dashed). The nondegenerate curves are a reproduction of those in Fig. 1(c) for the ^{87}Rb $F = 2$ hyperfine manifold with $B_{dc} = 11.98$ G and $\Omega_0 = 2\pi \times 1.224$ MHz. The degenerate ladder approximation sets $\Delta_{\{012\}} = 0$.

APPENDIX A: FIVE LEVEL DEGENERATE LADDER SYSTEM

For large rf field strengths ($|\Omega_0| \gg \Delta_{\{012\}}$), the five-level ladder system behaves as a degenerate ladder (i.e., $\Delta_{\{012\}} \rightarrow 0$), and the resonance substructure found from solving for the Hamiltonian given by Eq. (1) [see Fig. 1(c)] broadens into a single resonance. In this case, the ac Zeeman energy shifts are given by $E_{ACZ,\eta} = \eta \hbar [\frac{1}{4}(16\delta^2 + |\Omega_0|^2)^{1/2} - |\delta|]$ where $\eta = \{-2, -1, 0, +1, +2\}$ for the $\{-, -, 0, +, ++\}$ ACZ dressed states, respectively. Figure 8 shows the degenerate and nondegenerate ac Zeeman energy shifts for $B_{dc} = 11.98$ G. Finally, we note that the $E_{ACZ,\eta}$ energy shifts for the $\{-, 0, +\}$ dressed states are identical for the degenerate ladders of the $F = 2$ and $F = 1$ hyperfine manifolds.

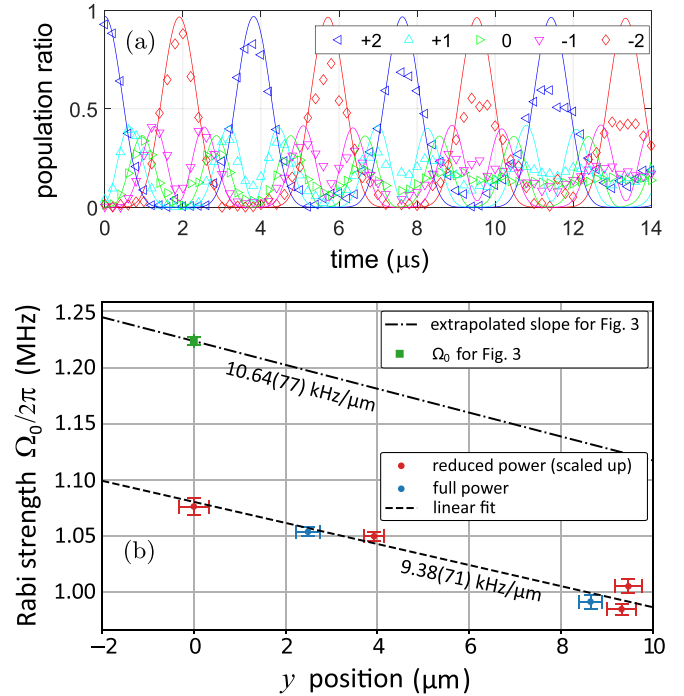


FIG. 9. Rabi strength Ω_0 and Rabi gradient $d\Omega_0/dy$ measurements. (a) Five-level Rabi flopping showing the fractional populations of the m_F states ($F = 2$) versus applied rf time to measure Ω_0 . The resonant rf is at 8.375 MHz with $B_{dc} = 11.98$ G. The solid lines are the result of a single least squares fit of the five populations based on a numerical model of the time evolution. The fit yields a Rabi strength of $\Omega_0 = 2\pi \times 1.05$ MHz. (b) Plot of Rabi strength Ω_0 versus atomic position for measuring $d\Omega_0/dy$. Rabi strength is measured at several positions relative to the original atomic cloud position by relaxing the ODT laser power so that the trap sags under gravity. The $y = 0$ position corresponds to the ODT trap center used for the Fig. 3 data. The Rabi flopping data are taken at two rf power levels, full power (blue points), and with the power reduced by -1.34 dB (red points), resulting in a measured gradient of $d\Omega_0/dy = 9.38 \pm 0.71$ kHz/ μm , based on a least squares linear fit (dashed line). The Rabi strength measured for the data used in Fig. 3 (green point) is larger than for the data used to measure the gradient, and so the corresponding slope has been scaled up to $d\Omega_0/dy = 10.64 \pm 0.77$ kHz/ μm (dash-dot line).

APPENDIX B: RABI FREQUENCY MEASUREMENT

The theory curves in Fig. 3 require measurements of the Rabi strength Ω_0 and its vertical gradient $d\Omega_0/dy$ as inputs. We measure Ω_0 directly by applying resonant rf at 8.375 MHz to $m_F = +2$ atoms in the ODT (with $B_{dc} = 12$ G) and then observing the Rabi flopping of all the m_F state populations as a function of the applied rf time [see Fig. 9(a)]. The Rabi flopping transfers the m_F state through the sequence $+2 \rightarrow +1 \rightarrow 0 \rightarrow -1 \rightarrow -2 \rightarrow -1 \rightarrow 0 \rightarrow +1 \rightarrow +2$ and then repeating. The flopping decoheres over time, in part due to a spatial gradient in the rf field strength across the trapped atomic cloud.

We compare the measured m_F population ratios against a numerical time evolution model based on the Schrödinger equation $i\hbar\partial|\psi(t)\rangle/\partial t = H_{\text{tot}}|\psi(t)\rangle$, where H_{tot} is given by Eq. (1). Here, $|\psi\rangle$ represents the spin state of an atom as a superposition of the five m_F states $|\psi\rangle = \sum_{j=m_F} c_j|j\rangle$. The fractional population in each m_F state is given by $P_j = |c_j|^2$. The solid lines in Fig. 9(a) represent a single fit of the time evolution of all five populations simultaneously with three parameters: Rabi strength Ω_0 , a modest initial $m_F = +1$ population, and a time delay offset. The fit does not include any decoherence (state mixing), although it is present in the data. Rabi strengths obtained at different rf powers \mathcal{P}_{rf} are compared by using the scaling relation $\Omega_0 \propto B_{\text{rf}} \propto I_{\text{rf}} \propto \sqrt{\mathcal{P}_{\text{rf}}}$.

We determine the vertical gradient $d\Omega_0/dy$ by measuring the Rabi strength Ω_0 at several different vertical y positions

[see red and blue data points in Fig. 9(b)]. The vertical position of the atoms is adjusted by up to 10 μm downwards by reducing the ODT laser power so that the trap center sags under gravity. We use a linear least squares fit to determine the slope $d\Omega_0/dy$. There is no obvious sign of curvature in the data, and so we do not include a quadratic term.

As shown in Fig. 9(b), the Ω_0 measurements for determining $d\Omega_0/dy$ were taken at full power (blue points) and also with the rf power reduced by 1.34 dB (red points). The Ω_0 measurements at reduced power are rescaled by $\sqrt{10^{1.34/10}}$ in Fig. 9(b) for comparison with the full power measurements.

The data in Fig. 3 and the data for measuring $d\Omega_0/dy$ [red and blue points in Fig. 9(b)] were both taken at the nominal full rf power but not on the same day. The green point in Fig. 9(b) shows the measured Rabi strength Ω_0 for the data taken in Fig. 3 and is about 13% larger than the corresponding red point at $y = 0$. We hypothesize that this discrepancy is due to rf amplifier power drift and vertical position drift of the ODT relative to the chip. In the case of a position change, a 13% increase in Ω_0 corresponds to the ODT being 15 μm closer to the chip: A position drift on this scale is consistent with observed ODT movement due to a room-temperature change of about 0.5° C, which is common. Due to the 13% higher Ω_0 for the data in Fig. 3, we scale $d\Omega_0/dy$ (obtained with red and blue points) by this same factor before applying it to Fig. 3.

-
- [1] M. Bloom, E. Enga, and H. Lew, Observation of the transverse Stern–Gerlach effect in neutral potassium, *Can. J. Phys.* **45**, 1481 (1967).
 - [2] R. J. C. Spreeuw, C. Gerz, L. S. Goldner, W. D. Phillips, S. L. Rolston, C. I. Westbrook, M. W. Reynolds, and I. F. Silvera, Demonstration of neutral atom trapping with microwaves, *Phys. Rev. Lett.* **72**, 3162 (1994).
 - [3] C. T. Fancher, A. J. Pyle, A. P. Rotunno, and S. Aubin, Microwave ac Zeeman force for ultracold atoms, *Phys. Rev. A* **97**, 043430 (2018).
 - [4] P. Böhi, M. F. Riedel, J. Hoffrogge, J. Reichel, T. W. Hänsch, and P. Treutlein, Coherent manipulation of Bose–Einstein condensates with state-dependent microwave potentials on an atom chip, *Nat. Phys.* **5**, 592 (2009).
 - [5] W. Miyahira, A. P. Rotunno, S. Du, and S. Aubin, Microwave atom chip design, *Atoms* **9**, 54 (2021).
 - [6] M. F. Riedel, P. Böhi, Y. Li, T. W. Hänsch, A. Sinatra, and P. Treutlein, Atom-chip-based generation of entanglement for quantum metrology, *Nature (London)* **464**, 1170 (2010).
 - [7] S. Du, A. R. Ziltz, W. Miyahira, and S. Aubin, Suppression of potential roughness in atom-chip ac Zeeman traps, *Phys. Rev. A* **105**, 053127 (2022).
 - [8] J. J. P. van Es, S. Whitlock, T. Fernholz, A. H. van Amerongen, and N. J. van Druten, Longitudinal character of atom-chip-based rf-dressed potentials, *Phys. Rev. A* **77**, 063623 (2008).
 - [9] T. Schumm, S. Hofferberth, L. M. Andersson, S. Wildermuth, S. Groth, I. Bar-Joseph, J. Schmiedmayer, and P. Krüger, Matter-wave interferometry in a double well on an atom chip, *Nat. Phys.* **1**, 57 (2005).
 - [10] B. M. Garraway and H. Perrin, Recent developments in trapping and manipulation of atoms with adiabatic potentials, *J. Phys. B: At., Mol. Opt. Phys.* **49**, 172001 (2016).
 - [11] R. A. Carollo, D. C. Aveline, B. Rhyno, S. Vishveshwara, C. Lannert, J. D. Murphree, E. R. Elliott, J. R. Williams, R. J. Thompson, and N. Lundblad, Observation of ultracold atomic bubbles in orbital microgravity, *Nature (London)* **606**, 281 (2022).
 - [12] Y. Guo, E. M. Gutierrez, D. Rey, T. Badr, A. Perrin, L. Longchambon, V. S. Bagnato, H. Perrin, and R. Dubessy, Expansion of a quantum gas in a shell trap, *New J. Phys.* **24**, 093040 (2022).
 - [13] A. P. Rotunno, Radiofrequency AC Zeeman trapping for neutral atoms, Ph.D. thesis, College of William and Mary, 2021; A. P. Rotunno, S. Du, W. Miyahira, and S. Aubin, Radio frequency ac Zeeman trapping on an atom chip, *Bull. Amer. Phys. Soc.* **66**(6), H09.00007 (2021).
 - [14] C. C. Agosta, I. F. Silvera, H. T. C. Stoof, and B. J. Verhaar, Trapping of neutral atoms with resonant microwave radiation, *Phys. Rev. Lett.* **62**, 2361 (1989).
 - [15] O. Zobay and B. M. Garraway, Recent developments in trapping and manipulation of atoms with adiabatic potentials, *Phys. Rev. Lett.* **86**, 1195 (2001).
 - [16] S. Hofferberth, B. Fischer, T. Schumm, J. Schmiedmayer, and I. Lesanovsky, Ultracold atoms in radio-frequency dressed potentials beyond the rotating-wave approximation, *Phys. Rev. A* **76**, 013401 (2007).

- [17] W. Ketterle and N. Van Druten, Evaporative cooling of trapped atoms, *Adv. At. Mol. Opt. Phys.* **37**, 181 (1996).
- [18] J. Dalibard and C. Cohen-Tannoudji, Dressed-atom approach to atomic motion in laser light: The dipole force revisited, *J. Opt. Soc. Am. B* **2**, 1707 (1985).
- [19] J. H. Shirley, Solution of the Schrödinger equation with a Hamiltonian periodic in time, *Phys. Rev.* **138**, B979 (1965).
- [20] H. Perrin and B. M. Garraway, Trapping atoms with radio frequency adiabatic potentials, *Adv. At. Mol. Opt. Phys.* **66**, 181 (2017).
- [21] M. K. Ivory, A. R. Ziltz, C. T. Fancher, A. J. Pyle, A. Sensharma, B. Chase, J. P. Field, A. Garcia, D. Jervis, and S. Aubin, Atom chip apparatus for experiments with ultracold rubidium and potassium gases, *Rev. Sci. Instrum.* **85**, 043102 (2014).
- [22] W. Gerlach and O. Stern, Der experimentelle Nachweis der Richtungsquantelung im Magnetfeld, *Eur. Phys. J. A* **9**, 349 (1922).
- [23] M. Bloom and K. Erdman, The transverse Stern–Gerlach experiment, *Can. J. Phys.* **40**, 179 (1962).
- [24] K. A. Burrows, H. Perrin, and B. M. Garraway, Nonadiabatic losses from radio-frequency-dressed cold-atom traps: Beyond the Landau-Zener model, *Phys. Rev. A* **96**, 023429 (2017).
- [25] M. W. Noel, W. M. Griffith, and T. F. Gallagher, Frequency-modulated excitation of a two-level atom, *Phys. Rev. A* **58**, 2265 (1998).